

Energy Efficiency Maximization for Hybrid RIS-Aided Communications via Deep Unfolding

Pouya Mobaraki, Graduate Student Member, IEEE, Abolfazl Zakeri, Member, IEEE, Marco Di Renzo, Fellow, IEEE, Markku Juntti, Fellow, IEEE, and Nhan Thanh Nguyen, Senior Member, IEEE

Abstract—We address energy-efficiency (EE) maximization in a multiuser (MU) multiple-input single-output (MISO) downlink system assisted by a hybrid reconfigurable intelligent surface (RIS), where each element can be dynamically configured to operate in either active or passive mode depending on whether its power amplifier is engaged. Practical hardware effects are explicitly incorporated, including base station (BS) and RIS power budgets, active-element amplifier gain limits, amplification noise, and binary phase control. To solve the problem, we develop an alternating-optimization framework in which the BS beamforming subproblem is handled via zero-forcing with closed-form power allocation, while the RIS subproblem is addressed using a model-driven deep unfolding approach. Numerical results show that the proposed method achieves faster convergence and higher EE than the considered benchmark schemes. In particular, it attains about 30% higher EE than the procedure without deep unfolding. Furthermore, our simulations demonstrate at least 10% EE improvement over the fully active RIS configuration and up to threefold EE gains compared with the fully passive RIS design. The results also show that most of the achievable EE gain can be captured by activating only a small fraction of RIS elements and allocating only a small portion of the dynamic power budget to the RIS.

I. Introduction

Reconfigurable intelligent surfaces (RISs) have attracted significant interest as a promising technology for future wireless systems due to their ability to modulate the wireless channel in a programmable manner [2], [3], [4]. By adjusting the phase of incident electromagnetic waves, RISs can redirect reflected signals toward intended users and improve coverage, spectral efficiency (SE), and energy efficiency (EE) [5]. However, when the incident signal is weak, conventional “passive” RIS cannot compensate for the severe multiplicative attenuation introduced by the cascaded transmitter–RIS–receiver channels. As a result, the received signal strength may become insufficient to guarantee reliable communications or the required quality of service (QoS) [6]. To overcome this limitation of passive RIS designs, “active” RIS architectures were introduced, in

which reflection-type amplifiers are integrated into the RIS to amplify the incoming signal before reflection, thereby alleviating cascaded channel attenuation [7].

However, equipping every RIS element with an amplifier significantly increases circuit power consumption, hardware complexity, and amplification noise. To achieve a balance among communication performance, power consumption, and hardware complexity, Nguyen et al. [8] introduced a “hybrid” RIS architecture, where only a subset of elements operate in active mode, while the remaining elements act as passive reflectors. Nevertheless, hybrid RIS design, particularly under the EE criterion, requires proper active element selection, since each active element needs a dedicated amplifier and additional circuit power. As a result, activating more elements increases total power consumption, while the corresponding improvement in communication performance (i.e., SE) may become negligible. This, in turn, leads to a noticeable reduction in the system EE.

EE optimization for hybrid RIS-assisted systems has recently been studied in [9], [10], [5], [11], [12], [13], [14], [15]. These works mainly employ conventional iterative methods, such as alternating optimization (AO), block coordinate descent, and successive convex approximation (SCA), and demonstrate the EE gains achievable with hybrid RIS. Nevertheless, several of these works assume that the active/passive operating mode of each RIS element is predetermined, rather than optimized as part of the system design. This assignment directly shapes the cascaded channel and, consequently, the achievable EE. However, jointly optimizing the active/passive mode assignment with the continuous beamforming and RIS coefficients renders the problem computationally demanding and leads to slow convergence under conventional iterative methods. Motivated by this, we address the EE maximization problem for hybrid RIS-assisted communications, where each RIS element is selected to operate either in active or passive mode, using a model-driven deep unfolding approach [16], [17].

We consider a hybrid RIS-assisted multiuser (MU) multiple-input single-output (MISO) downlink system, as illustrated in Fig. 1. Our objective is to jointly design the transmit beamforming at the BS, the set of RIS elements operating in the active mode along with their amplification gains, and the phase shifts of all RIS elements to maximize the system EE. The design is subject to the BS and RIS power budgets, per-user minimum-SE QoS constraints, the

Pouya Mobaraki, Abolfazl Zakeri, Markku Juntti, and Nhan Thanh Nguyen are with the Centre for Wireless Communications, University of Oulu, P.O. Box 4500, FI-90014 Oulu, Finland (e-mail: {pouya.mobaraki, abolfazl.zakeri, markku.juntti, nhan.nguyen}@oulu.fi). Marco Di Renzo is with CNRS, Centrale-Supélec, Laboratoire des Signaux et Systèmes, Université Paris-Saclay, 91192 Gif-sur-Yvette, France, and also with the Centre for Telecommunications Research, Department of Engineering, King’s College London, WC2R 2LS London, U.K. (e-mail: marco.i.di_renzo@kcl.ac.uk).

The preliminary results of this paper are presented [1].

BS and RIS power consumption models, and binary phase-shift constraints of the RIS elements.

The resulting problem is a mixed-integer non-convex optimization problem with a fractional EE objective, coupled variables, non-convex constraints, and discrete active-element set selection. To address this, we propose two methods. Our primary method employs an AO framework to decouple the problem into two parts: BS beamforming and RIS optimization. The BS beamforming part is solved via a zero-forcing (ZF) beamformer, with power allocation obtained in closed form using the Dinkelbach technique. For the RIS optimization part, we propose a model-driven deep unfolding approach in which the iterations of the projected gradient method are unrolled into trainable layers, with smoothing and relaxation techniques introduced to enable differentiable treatment of the discrete active-element selection and binary phase-shift constraints. As a benchmark, the second method applies conventional projected gradient ascent (PGA), where all optimization variables are jointly updated through gradient ascent iterations with projection onto the feasible sets; the QoS constraints are enforced via a barrier penalty incorporated into the objective.

We conduct extensive simulations to evaluate the proposed deep unfolding-based AO method and the PGA benchmark, alongside different RIS architectures, including fully passive and fully active RISs. We further analyze the impact of key system parameters on EE, including the number of active elements and the power budget allocation between the BS and the RIS.

Our main contributions are summarized as follows:

- We address an EE maximization problem for a hybrid RIS-assisted MU-MISO downlink system by jointly optimizing the active/passive mode selection, BS beamforming, and RIS coefficients.
- We develop a model-driven deep unfolding approach for the joint active-element selection and RIS coefficient optimization subproblem, with smoothing and relaxation techniques to handle the discrete and binary variables.
- We further develop a PGA-based method that jointly updates all optimization variables through gradient ascent with barrier-penalty enforcement of the QoS constraints.
- We conduct numerical results demonstrating that the proposed deep unfolding-based AO method achieves nearly fourfold improvement over the PGA-based method. Furthermore, the hybrid RIS outperforms both fully passive and fully active RIS architectures, and activating only 10% of the elements suffices to achieve approximately 80% of the maximum EE.

Organization: The rest of this paper is organized as follows. Section II reviews the related work. Section III presents the system model and problem formulation. Section IV presents the proposed deep unfolded AO methods to solve the resulting problem. Section V presents the PGA-based solution to the main problem. Simulation

results are provided in Section VI, followed by the conclusions in Section VII.

Notations: Scalars, vectors, matrices, and sets are denoted by lower-case letters, bold-face lower-case letters, bold-face upper-case letters, and calligraphic upper-case letters, respectively. The conjugate and conjugate transpose are respectively denoted by $(\cdot)^*$ and $(\cdot)^H$. Additionally, $\mathbb{C}^{m \times n}$ denotes the set of $m \times n$ complex-valued matrices. \mathbf{I}_N denotes the $N \times N$ identity matrix, and $\text{diag}\{a_1, \dots, a_N\}$ denotes a diagonal matrix with diagonal entries a_1, \dots, a_N . The operators $\text{tr}(\cdot)$ and ∇ denote the trace and gradient, respectively. Moreover, $|\cdot|$ denotes the absolute value of a scalar, $\|\cdot\|$ denotes the Euclidean norm, and $\|\cdot\|_F$ denotes the Frobenius norm. The cardinality of a set \mathcal{B} is denoted by $|\mathcal{B}|$, and $\mathbb{1}_N^{\mathcal{A}}$ denotes the N -dimensional indicator vector associated with the set \mathcal{A} . Finally, $\mathcal{CN}(\mathbf{0}, \mathbf{C})$ denotes the circularly symmetric complex Gaussian distribution with zero mean and covariance matrix \mathbf{C} .

II. Related Work

Hybrid RIS-assisted transmission design has been extensively studied under a range of system configurations and performance metrics [8], [18], [19], [20], [21], [22]. In [8], a hybrid RIS-assisted multiple-input multiple-output (MIMO) system was considered and solved using an AO framework with SCA. The results showed that employing only a small number of active elements can significantly improve SE compared with fully passive RIS designs. Similarly, [18] investigated weighted sum-rate maximization in an MU-MIMO system using an SCA-based AO approach. Their results showed that a hybrid RIS can balance the beamforming gain of a fully passive RIS and the power amplification gain of a fully active RIS, while mitigating the multiplicative path-loss effect. The work in [19] analyzed the max-min ergodic capacity of a hybrid RIS-assisted multiuser system under Rician fading with statistical CSI, by optimizing the RIS phase shifts, amplification coefficients, and active-element positions. In [20], a hybrid RIS-assisted unmanned aerial vehicle (UAV) communication system was studied, where BCA and SCA were used to maximize the minimum user rate through joint optimization of the UAV trajectory and RIS coefficients.

Beyond SE, EE in RIS-assisted systems has also received considerable attention [5], [10], [11], [12], [13], [14], [15], [23], [24]. In [5], EE was maximized for a fully passive RIS-assisted MU-MISO downlink system using fractional programming within an AO framework. For hybrid RIS systems, the works in [10], [11], [12] investigated EE maximization under different system settings. Specifically, in [10], a cell-free network was studied, and the results showed that a small number of active elements can outperform both fully passive and fully active architectures. In [11], a massive MIMO system with hardware impairments was considered using an AO-based design. In [12], RIS mode switching together with amplitude and phase control was optimized within an AO framework

using the Dinkelbach method. Overall, these works rely on conventional iterative methods and demonstrate the EE potential of hybrid RIS. However, they do not explicitly address active/passive mode selection, which is important for EE design because it directly affects both the effective cascaded channel and the overall power consumption.

One important aspect of hybrid RIS system design is the incorporation of practical hardware constraints, particularly low-resolution phase control. In this regard, one-bit phase shifts have been widely recognized as a cost-effective and energy-efficient solution for practical RIS implementation [25]. For example, [26] investigated discrete phase-shift design for an RIS-assisted system and proposed efficient quantization methods, showing that low-resolution phase control can still provide substantial beamforming gains with robust performance. Beyond phase-shift design, the active/passive element assignment can also significantly affect system performance, especially from the EE perspective. In [27], the rate, EE, and their trade-off were optimized with respect to the number and phase shifts of RIS elements while accounting for channel-estimation and RIS-configuration overheads. In [28], both fixed and dynamic hybrid RIS architectures were studied for secure communications in a MISO system with a multi-antenna eavesdropper, where the BS transmit covariance matrix, the reflection matrices of the active and passive sub-RISs, and the element allocation matrix were jointly optimized to maximize the secrecy rate. Similarly, [21] considered a hybrid RIS with flexible active/passive mode switching in a mobile edge computing system and showed that the element assignment critically affects the latency-energy trade-off.

Nevertheless, jointly optimizing binary phase-shift design and active/passive mode selection introduces significant challenges that render conventional optimization methods difficult to apply, especially in large-scale systems. To address such difficulties, data-driven approaches based on deep neural networks have been proposed for RIS optimization [29]. However, these methods often suffer from limited interpretability, dependence on large training datasets, and lack of performance guarantees, since the learned mappings are not explicitly tied to the underlying problem structure [30]. In contrast, model-based deep learning, and deep unfolding in particular, provides a more principled framework by embedding the iterations of an optimization algorithm into trainable neural network layers [16], [31], [17]. In this way, it preserves the problem structure, improves interpretability, and can achieve faster convergence with fewer trainable parameters. Deep unfolding has already been applied to RIS-assisted systems for problems such as transmit beamforming and joint active/passive coefficient design, where it has shown faster convergence and lower complexity than purely iterative methods [32], [33]. However, its use for EE maximization in hybrid RIS systems with active-element set selection and binary phase-shift constraints remains largely unexplored. In our problem, these constraints make the optimization combinatorial and prevent the direct use

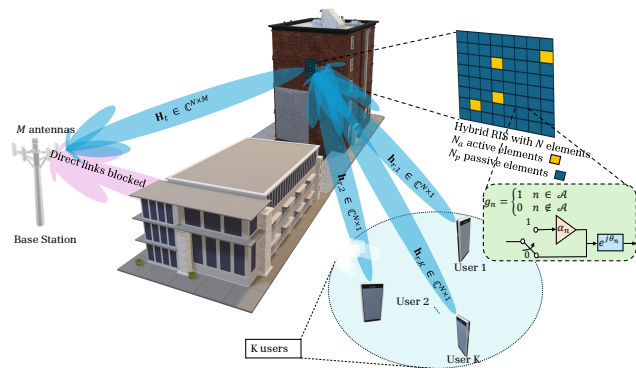


Fig. 1. Considered hybrid RIS-assisted MU-MISO downlink system.

of standard gradient-based deep unfolding steps due to their non-differentiability. This is the gap addressed in this work.

III. System Model and Problem Formulation

A. System Model

We consider a hybrid RIS-assisted MU-MISO downlink system, as illustrated in Fig. 1. The BS is equipped with M transmit antennas and serves K single-antenna users. The set of users is denoted by $\mathcal{K} = \{1, \dots, K\}$. The direct links from the BS to the users are assumed to be blocked, and communications are established through a hybrid RIS composed of N elements. In the hybrid RIS, N_a elements are active and can both reflect and amplify incident signals, while the remaining $N - N_a$ elements are passive, which can only reflect signals.

Let $\theta_n \in \{0, \pi\}$ denote the binary phase shift of hybrid RIS element n , for $n = 1, \dots, N$. Furthermore, let $\mathcal{N} = \{1, \dots, N\}$ and $\mathcal{A} \subset \mathcal{N}$ denote the set of RIS elements and the subset of active elements, with $|\mathcal{N}| = N$ and $|\mathcal{A}| = N_a$, respectively. We denote the overall hybrid RIS coefficient matrix by the diagonal matrix Φ ,

$$\Phi = \text{diag} \{ \phi_1, \dots, \phi_N \}, \quad (1)$$

where each diagonal element ϕ_n is given by

$$\phi_n = \begin{cases} \alpha_n e^{j\theta_n}, & n \in \mathcal{A} \text{ (active element)}, \\ e^{j\theta_n}, & n \notin \mathcal{A} \text{ (passive element)}. \end{cases} \quad (2)$$

Here, α_n denotes the real-valued amplitude coefficient of the n th active element ($1 \leq \alpha_n \leq \alpha^{\max}$), where α^{\max} represents the maximum amplification gain. Based on (2), we decompose Φ into two diagonal matrices, Φ_a and Φ_p , which represent the active and passive reflection coefficients, respectively, i.e.,

$$\Phi = \underbrace{\text{diag} \{ \mathbb{1}_N^{\mathcal{A}} \}}_{\triangleq \Phi_a} \Phi + \underbrace{(\mathbb{I}_N - \text{diag} \{ \mathbb{1}_N^{\mathcal{A}} \})}_{\triangleq \Phi_p} \Phi, \quad (3)$$

where $\mathbb{1}_N^{\mathcal{A}}$ is an indicator vector of dimension N with ones at the positions corresponding to the active element set \mathcal{A} . This decomposition is introduced to explicitly separate the contributions of the active and passive elements in the subsequent analysis.

Let $\mathbf{x} = [x_1, \dots, x_K]^\top \in \mathbb{C}^{K \times 1}$ be the vector of transmitted symbols at the BS, with $\mathbb{E}\{\mathbf{x}\mathbf{x}^H\} = \mathbf{I}_K$. Furthermore, let $\mathbf{F} = [\mathbf{f}_1, \dots, \mathbf{f}_K] \in \mathbb{C}^{M \times K}$ be the transmit beamforming matrix. The transmitted signal from the BS is given by $\mathbf{s} = \mathbf{F}\mathbf{x}$. The received signal at user k , denoted by y_k , can be expressed as

$$y_k = \mathbf{h}_{r,k}^H \Phi \mathbf{H}_t \mathbf{F} \mathbf{x} + \mathbf{h}_{r,k}^H \Phi_a \mathbf{z}_R + z_k, \quad (4)$$

where $\mathbf{H}_t \in \mathbb{C}^{N \times M}$ and $\mathbf{h}_{r,k} \in \mathbb{C}^N$ denote the channels between the BS and the RIS and between the RIS and user k , respectively. We assume that perfect CSI is available at the BS. In (4), $z_k \sim \mathcal{CN}(0, \sigma_k^2)$ denotes the additive white Gaussian noise (AWGN) at user k , while $\mathbf{z}_R \sim \mathcal{CN}(0, \sigma_R^2 \mathbf{I}_N)$ is the thermal noise introduced by the active elements at the hybrid RIS.

Assume that the symbol x_k is intended for user k . The signal-to-interference-plus-noise ratio (SINR) at this user is given by

$$\gamma_k = \frac{|\mathbf{h}_{r,k}^H \Phi \mathbf{H}_t \mathbf{f}_k|^2}{\sum_{i \neq k} |\mathbf{h}_{r,k}^H \Phi \mathbf{H}_t \mathbf{f}_i|^2 + \sigma_k^2 + \sigma_R^2 \|\mathbf{h}_{r,k}^H \Phi_a\|^2}. \quad (5)$$

Thus, the SE of user k is given by $\text{SE}_k = \log_2(1 + \gamma_k)$, and the total SE of the system is

$$\text{SE} = \sum_{k \in \mathcal{K}} \text{SE}_k. \quad (6)$$

B. Problem Formulation

Our objective is to maximize the system EE, defined as the ratio between the SE and the total power consumption. We first present the power consumption model of the considered system.

1) Power Model: The overall power consumption in the considered system consists of two components: 1) the power consumption at the BS and 2) the power consumption at the hybrid RIS. The overall BS power consumption is modeled as [34]¹

$$P_{\text{BS}} = \frac{1}{\xi} P_t + P_{c,\text{BS}}, \quad (7)$$

where $\xi \in (0, 1]$ denotes the power amplifier efficiency, $P_t = \text{tr}(\mathbf{F}\mathbf{F}^H)$ is the BS transmit power, and $P_{c,\text{BS}}$ represents the static circuit power.

For the hybrid RIS with N reflecting elements, each element requires a phase shifter, leading to a power consumption of NP_{ps} , where P_{ps} is the power consumed by one phase shifter. Active elements further incur amplifier-related power consumption, consisting of a static bias power P_{dc} required to keep the amplifier active [9], and a dynamic power term P_r , which denotes the output power of the active RIS elements and accounts for both the amplified incident signal and the amplified thermal noise

$$P_r = \text{tr}(\Phi_a \mathbf{H}_t \mathbf{F} \mathbf{F}^H \mathbf{H}_t^H \Phi_a^H) + \text{tr}(\sigma_R^2 \Phi_a \Phi_a^H). \quad (8)$$

¹Notice that the users' power consumption is not included in the BS power consumption, similarly to [35]. It can be readily added (as a constant term) in the total power consumption model.

Combining these terms, the total hybrid RIS power consumption is given by

$$P_{\text{RIS}} = NP_{\text{ps}} + N_a P_{\text{dc}} + \frac{1}{\zeta} P_r, \quad (9)$$

where $\zeta \in (0, 1]$ denotes the amplifier efficiency at the RIS active elements. Finally, the overall system power consumption of the considered hybrid RIS-aided system is given by

$$P_{\text{tot.}} = P_{\text{BS}} + P_{\text{RIS}} = \frac{1}{\xi} P_t + \frac{1}{\zeta} P_r + P_c, \quad (10)$$

where $P_c \triangleq P_{c,\text{BS}} + NP_{\text{ps}} + N_a P_{\text{dc}}$ denotes the total static power consumption of the BS and RIS.

2) EE Design Problem: We aim to jointly design the BS beamforming matrix \mathbf{F} , the hybrid RIS reflection matrix Φ , and the active-element set \mathcal{A} to maximize the system EE under the BS and RIS power budgets, the QoS, and hardware limitations, including the amplification limits of the active elements, binary phase-shift control, and the fixed active-element cardinality. Mathematically, this problem is formulated as

$$\underset{\mathbf{F}, \Phi, \mathcal{A}}{\text{maximize}} \quad \text{EE} \triangleq \frac{\text{SE}}{P_{\text{tot.}}} \quad (11a)$$

$$\text{subject to} \quad \text{tr}(\mathbf{F}\mathbf{F}^H) \leq P_t^{\text{max}}, \quad (11b)$$

$$P_r \leq P_r^{\text{max}}, \quad (11c)$$

$$\text{SE}_k \geq \text{SE}_k^{\text{min}}, \quad \forall k \in \mathcal{K}, \quad (11d)$$

$$1 \leq \alpha_n \leq \alpha_n^{\text{max}}, \quad \forall n \in \mathcal{A}, \quad (11e)$$

$$\theta_n \in \{0, \pi\}, \quad \forall n \in \mathcal{N}, \quad (11f)$$

$$|\mathcal{A}| = N_a, \quad (11g)$$

where P_t^{max} and P_r^{max} are the transmit power budget at the BS and the hybrid RIS, respectively, and SE_k^{min} denotes the minimum SE requirement of user k . Constraints (11b) and (11c) impose the transmit power limitations at the BS and the hybrid RIS, respectively. Constraint (11d) ensures the QoS requirement of each user by enforcing a minimum SE level. Furthermore, constraint (11e) restricts the amplitude coefficients of the active RIS elements to their feasible range. Constraint (11f) imposes binary phase-shift control for each RIS element, and (11g) limits the total number of active elements.

The EE maximization problem in (11) is a non-convex mixed-integer program. The main challenges arise from the fractional and non-convex objective function in (11a), the coupling among the beamforming and RIS design variables in both the SE and power-consumption expressions, and the discrete nature of the RIS design variables. In particular, the selection of the active-element set \mathcal{A} is combinatorial, while constraints (11c)–(11g) are difficult to handle due to the RIS power constraint, QoS requirements, binary phase-shift control, and active-element selection. Therefore, solving (11) optimally is highly challenging. In the next section, we present an efficient solution based on AO and deep unfolding.

IV. Proposed Deep Unfolded Alternating Optimization Method

In this section, we present our proposed solution to the EE maximization problem in (11). We adopt an AO framework and decouple the original problem into two subproblems. The BS beamforming and power allocation subproblem, with fixed RIS parameters, is solved in closed form and detailed in Section IV-B1. The hybrid RIS optimization subproblem, with fixed BS variables, is then handled using a model-driven deep unfolding method in Section IV-B2.

Before applying AO, we employ ZF beamforming to cancel the multiuser interference terms and simplify the SINR expression in (5). With ZF, the beamforming matrix is given by

$$\mathbf{F} = \mathbf{H}(\mathbf{H}^H\mathbf{H})^{-1}\mathbf{P}^{\frac{1}{2}} \triangleq \mathbf{H}^\dagger\mathbf{P}^{\frac{1}{2}}, \quad (12)$$

where $\mathbf{H}^H \triangleq \mathbf{H}_r^H\mathbf{\Phi}\mathbf{H}_t$ denotes the cascaded channel from the BS to the users, $\mathbf{H}_r = [\mathbf{h}_{r,1}, \mathbf{h}_{r,2}, \dots, \mathbf{h}_{r,K}] \in \mathbb{C}^{N \times K}$ collects the channels between the hybrid RIS and the users, and $\mathbf{H}^\dagger \triangleq \mathbf{H}(\mathbf{H}^H\mathbf{H})^{-1}$. Matrix \mathbf{P} is given by $\mathbf{P} = \text{diag}\{p_1, \dots, p_K\}$, where p_k denotes the power allocation factor associated with user k . In the following, we reformulate problem (11) under the ZF beamforming structure.

A. Reformulation of (11) with ZF Beamforming

With ZF, the SINR of user k in (5) can be rewritten as

$$\gamma_k = \frac{p_k}{\sigma_k^2 + \sigma_R^2 \left\| \mathbf{h}_{r,k}^H \mathbf{\Phi}_a \right\|^2}. \quad (13)$$

Furthermore, the BS transmit power P_t and the hybrid RIS dynamic amplifier power P_r , respectively, become

$$P_t = \text{tr} \left(\mathbf{P}^{\frac{1}{2}} (\mathbf{H}^H\mathbf{H})^{-1} \mathbf{P}^{\frac{1}{2}} \right) = \text{tr} \left(\mathbf{P} (\mathbf{H}^H\mathbf{H})^{-1} \right), \quad (14)$$

$$P_r(\mathbf{\Phi}_a, \mathbf{P}) = \text{tr} \left(\mathbf{\Phi}_a \mathbf{H}_t \mathbf{H}^\dagger \mathbf{P} (\mathbf{H}^\dagger)^H \mathbf{H}_t^H \mathbf{\Phi}_a^H \right) + \text{tr} \left(\sigma_R^2 \mathbf{\Phi}_a \mathbf{\Phi}_a^H \right). \quad (15)$$

As a result, the system EE is now given by

$$\text{EE} = \frac{\sum_{k=1}^K \log_2 \left(1 + \frac{p_k}{\sigma_k^2 + \sigma_R^2 \left\| \mathbf{h}_{r,k}^H \mathbf{\Phi}_a \right\|^2} \right)}{\frac{1}{\xi} P_t + P_c + \frac{1}{\zeta} P_r(\mathbf{\Phi}_a, \mathbf{P})}. \quad (16)$$

The new design objective in (16) is still highly complicated because $\mathbf{\Phi}_a$ and \mathbf{P} appear in the denominators of both the SINR and EE expressions. This renders the problem fractional and non-convex, making it highly challenging to solve directly. In particular, the dynamic amplifier power depends on the RIS coefficients in a highly nonlinear manner, while the noise introduced by the active RIS elements appears as an additional term in the SINR denominator. These coupled nonlinearities make

the problem intractable in its current form.

To overcome this challenge, we make the following observations. First, the noise power at user k introduced by the active RIS elements, i.e., $\sigma_R^2 \left\| \mathbf{h}_{r,k}^H \mathbf{\Phi}_a \right\|^2$, is negligible compared with σ_k^2 , since σ_R^2 and σ_k^2 are of comparable magnitude [34], whereas the severe RIS-to-user path loss yields $\left\| \mathbf{h}_{r,k}^H \mathbf{\Phi}_a \right\|^2 \ll 1$. Thus, this term can be omitted from the SINR expression to make the objective function more tractable. Second, the amplifier power at the active RIS elements in the denominator of the EE, i.e., $P_r(\mathbf{\Phi}_a, \mathbf{P})$, is much smaller than the power components at the BS, since the RIS operates under a significantly more limited power budget than the BS [34]. Hence, its impact on the EE is limited.

Based on the above observations, we consider the following approximation of the EE, denoted by $\widetilde{\text{EE}}$

$$\widetilde{\text{EE}} = \frac{\sum_{k=1}^K \log_2 \left(1 + \frac{p_k}{\sigma_k^2} \right)}{\frac{1}{\xi} P_t + P_c + \frac{1}{\zeta} P_r^{\text{max}}}, \quad (17)$$

where the term $\sigma_R^2 \left\| \mathbf{h}_{r,k}^H \mathbf{\Phi}_a \right\|^2$ is removed from the SINR denominator, and $P_r(\mathbf{\Phi}_a, \mathbf{P})$ is replaced by its maximum allowable value P_r^{max} based on constraint (11c). The approximation becomes tight when the RIS uses most of its available power budget for signal amplification and when the RIS power budget is relatively small compared with the BS-side power consumption. This aligns with practical systems, where RISs operate under low-power conditions. In the simulation results, we also quantify the approximation accuracy by comparing $\widetilde{\text{EE}}$ with the original EE in (16).

As a result, problem (11) can be reformulated as

$$\underset{\mathbf{P}, \mathbf{\Phi}, \mathcal{A}}{\text{maximize}} \quad \widetilde{\text{EE}}, \quad (18a)$$

$$\text{subject to} \quad \text{tr} \left(\mathbf{P} (\mathbf{H}^H\mathbf{H})^{-1} \right) \leq P_t^{\text{max}}, \quad (18b)$$

$$P_r \leq P_r^{\text{max}}, \quad (18c)$$

$$p_k \geq \sigma_k^2 (2^{\text{SE}_k^{\text{min}}} - 1), \quad \forall k \in \mathcal{K}, \quad (18d)$$

$$(11e) - (11g). \quad (18e)$$

The resulting optimization problem remains non-convex. We next present its solution.

B. AO Method

In the AO framework, the power allocation matrix \mathbf{P} and the hybrid RIS coefficients $(\mathbf{\Phi}, \mathcal{A})$ are optimized in an alternating manner by solving two corresponding subproblems while keeping the other variables fixed, as detailed below.

1) Power Allocation Subproblem: For a given hybrid RIS coefficient matrix $\mathbf{\Phi}$ and active set \mathcal{A} , problem (18) can be rewritten as

$$\underset{\mathbf{P}}{\text{maximize}} \quad \frac{\sum_{k=1}^K \log_2 \left(1 + \frac{p_k}{\sigma_k^2} \right)}{\bar{P} + \frac{1}{\xi} \sum_{k=1}^K p_k t_k}, \quad (19a)$$

$$\text{subject to } \sum_{k=1}^K p_k t_k \leq P_t^{\max}, \quad (19b)$$

$$\sum_{k=1}^K p_k d_k + \text{tr} \left(\sigma_R^2 \Phi_a \Phi_a^H \right) \leq P_r^{\max}, \quad (19c)$$

$$p_k \geq p_k^{\min}, \quad \forall k \in \mathcal{K}, \quad (19d)$$

where $\bar{P} \triangleq P_c + \frac{1}{\xi} P_r^{\max}$ and $p_k^{\min} \triangleq \sigma_k^2 (2^{\text{SE}_k^{\min}} - 1)$ are constants. Furthermore, t_k and d_k are the k th diagonal elements of $(\mathbf{H}^H \mathbf{H})^{-1}$ and $(\mathbf{H}^\dagger)^H \mathbf{H}_t^H \Phi_a^H \Phi_a \mathbf{H}_t \mathbf{H}^\dagger$, respectively.

Although all constraints (19b)–(19d) are convex, the objective in (19a) is fractional and hence non-concave. To solve problem (19), we employ the Dinkelbach method [36], which iteratively solves the following problem in iteration $(i+1)$

$$\underset{\mathbf{P}}{\text{maximize}} f(\mathbf{P}), \text{ subject to (19b)–(19d)}, \quad (20)$$

where $f(\mathbf{P}) \triangleq \sum_{k=1}^K \log_2 \left(1 + \frac{p_k}{\sigma_k^2} \right) - \lambda^{(i)} \left(\bar{P} + \frac{1}{\xi} \sum_{k=1}^K p_k t_k \right)$ and

$$\lambda^{(i)} \triangleq \frac{\sum_{k=1}^K \log_2 \left(1 + \frac{p_k^{(i)}}{\sigma_k^2} \right)}{\bar{P} + \frac{1}{\xi} \sum_{k=1}^K p_k^{(i)} t_k} \quad (21)$$

denotes the Dinkelbach parameter, which is updated from the solution of the problem in the previous iteration i , i.e., $\mathbf{P}^{(i)*} = [p_k^{(i)}]$. Problem (20) is convex, and its closed-form solution is derived as follows.

The Lagrangian of (20) can be written as

$$\begin{aligned} \mathcal{L}(\mathbf{P}, \boldsymbol{\mu}) &= \mu_0 \left(\sum_{k=1}^K p_k t_k - P_t^{\max} \right) - \sum_{k=1}^K \mu_k (p_k - p_k^{\min}) \\ &\quad + \mu_{K+1} \left(\sum_{k=1}^K p_k d_k - \hat{P}_r^{\max} \right) - f(\mathbf{P}). \end{aligned} \quad (22)$$

where $\hat{P}_r^{\max} = P_r^{\max} - \text{tr}(\sigma_R^2 \Phi_a \Phi_a^H)$ is introduced for notational simplicity and $\{\mu_k\}_{k=0}^{K+1}$ are the dual variables, $\mu_k \geq 0, \forall k$. Then, the KKT conditions of (22) include

$$g(\mu_0, \mu_{K+1}) - \mu_k = \frac{1}{(p_k + \sigma_k^2) \ln 2}, \quad \forall k \in \mathcal{K}, \quad (23a)$$

$$\mu_0 \left(\sum_{k=1}^K p_k t_k - P_t^{\max} \right) = 0, \quad (23b)$$

$$\mu_{K+1} \left(\sum_{k=1}^K p_k d_k - \hat{P}_r^{\max} \right) = 0, \quad (23c)$$

$$\mu_k (p_k - p_k^{\min}) = 0, \quad \forall k \in \mathcal{K}, \quad (23d)$$

where $g(\mu_0, \mu_{K+1}) \triangleq \left(\frac{\lambda^{(i)}}{\xi} + \mu_0 \right) t_k + \mu_{K+1} d_k$. By substituting (23d) into (23a), we obtain

$$p_k = \max \left\{ \frac{1}{g(\mu_0, \mu_{K+1}) \ln 2} - \sigma_k^2, p_k^{\min} \right\}. \quad (24)$$

Algorithm 1 Dinkelbach Algorithm for Solving Power Allocation Subproblem (20)

Require: \mathbf{H} and Φ_a

- 1: Obtain t_k and d_k as the k -th diagonal elements of $(\mathbf{H}^H \mathbf{H})^{-1}$ and $(\mathbf{H}^\dagger)^H \mathbf{H}_t^H \Phi_a^H \Phi_a \mathbf{H}_t \mathbf{H}^\dagger$, respectively.
 - 2: Initialize $\lambda^{(0)} > 0, i = 1$.
 - 3: repeat
 - 4: Find μ_0^*, μ_{K+1}^* satisfying (25a), (25b) via bisection search.
 - 5: Update power allocation $p_k^{(i)} \leftarrow p_k(\mu_0^*, \mu_{K+1}^*), \forall k$
 - 6: Update Dinkelbach factor based on (21).
 - 7: $i \leftarrow i + 1$
 - 8: until convergence
 - 9: return $\{p_k^*\} \leftarrow \{p_k^{(i)}\}$
-

It is observed from (24) that p_k is a function of the dual variables μ_0 and μ_{K+1} , together with the complementary slackness conditions in (23b)–(23c), the optimal dual variables μ_0 and μ_{K+1} are determined such that the following conditions are satisfied

$$\sum_{k=1}^K t_k p_k(\mu_0, \mu_{K+1}) \leq P_t^{\max}, \quad (25a)$$

$$\sum_{k=1}^K d_k p_k(\mu_0, \mu_{K+1}) \leq \hat{P}_r^{\max}, \quad (25b)$$

$$\mu_0 \left(\sum_{k=1}^K t_k p_k(\mu_0, \mu_{K+1}) - P_t^{\max} \right) = 0, \quad (25c)$$

$$\mu_{K+1} \left(\sum_{k=1}^K d_k p_k(\mu_0, \mu_{K+1}) - \hat{P}_r^{\max} \right) = 0, \quad (25d)$$

Since $p_k(\mu_0, \mu_{K+1})$ is monotonically non-increasing with respect to both μ_0 and μ_{K+1} , the constraints in (25a) and (25b) define monotone functions of the dual variables. Therefore, the optimal (μ_0^*, μ_{K+1}^*) can be efficiently obtained via a bisection search, where for a fixed μ_{K+1} , the value of μ_0 is uniquely determined such that (25a) holds with equality if active, and μ_{K+1} is subsequently updated to satisfy (25b). This procedure is repeated iteratively until convergence, as summarized in Algorithm 1.

2) RIS Optimization Subproblem: With \mathbf{P} fixed in problem (18), we aim to solve for Φ and \mathcal{A} . Note that the numerator of the objective function is independent of Φ and \mathcal{A} , and only the BS transmit power in (14) depends on Φ and \mathcal{A} , while other power consumption components remain constant. Based on these observations, the hybrid RIS optimization in (18) can be formulated as

$$\underset{\Phi, \mathcal{A}}{\text{minimize}} f(\Phi) \triangleq \text{tr}(\mathbf{P}(\mathbf{H}^H \mathbf{H})^{-1}), \quad (26a)$$

$$\text{subject to } \text{tr}(\mathbf{P}(\mathbf{H}^H \mathbf{H})^{-1}) \leq P_t^{\max}, \quad (26b)$$

$$P_r \leq P_r^{\max}, \quad (26c)$$

$$(11e) - (11g). \quad (26d)$$

The above problem is a combinatorial optimization problem with a highly non-convex and discrete set of variables, which is generally NP-hard and not solvable in polynomial time. We propose an efficient solution based on this problem by leveraging PGD and deep unfolding.

a) PGD Framework: In the PGD framework, Φ is updated at iteration $j + 1$ as

$$\Phi^{(j+1)} = \mathcal{P}\left(\Phi^{(j)} - \eta_{\Phi}^{(j)} \nabla_{\Phi} f(\Phi^{(j)})\right), \quad (27)$$

where $\eta_{\Phi}^{(j)}$ denotes the step size at the j th iteration, and $\mathcal{P}(\cdot)$ represents the projection operator that ensures feasibility. To compute the gradient $\nabla_{\Phi} f(\Phi^{(j)})$, we first relax the binary phase-shift variables and assume that the RIS is fully active, i.e., $\mathcal{A} \equiv \mathcal{N}$ and $\theta_n \in [0, \pi]$ in (2). This relaxation is necessary because the discrete phase-shift coefficients are non-differentiable, which prevents the direct application of gradient-based optimization methods. Under this relaxation, $\nabla_{\Phi} f(\Phi^{(j)})$ is given by

$$\nabla f(\Phi) = -2(\mathbf{H}_r(\mathbf{H}^H \mathbf{H})^{-1} \mathbf{P}(\mathbf{H}^\dagger)^H \mathbf{H}_t^H) \circ \mathbf{I}_N, \quad (28)$$

where the Hadamard product (\circ) with \mathbf{I}_N is to ensure the dimensionality [37].

To guarantee feasibility, the projection operator $\mathcal{P}(\cdot)$ in (27) is implemented sequentially. First, the phase of each RIS coefficient is quantized to the binary set $\{0, \pi\}$ to satisfy the discrete phase-shift constraint in (11f). Next, the active set \mathcal{A} is determined by selecting the N_a elements with the largest amplitudes in accordance with (11g), while the remaining elements are assigned as passive. Subsequently, the amplitudes of the selected active elements are clipped to the feasible interval defined by (11e). Finally, if the maximum dynamic amplifier power constraint in (26c) is violated, the active RIS coefficients are rescaled to satisfy this constraint. The obtained solution is then checked against the BS transmit power constraint in (26b).

b) Deep Unfolded PGD: In the PGD method, the step-size sequence $\{\eta_{\Phi}^{(j)}\}_{j=0}^{J-1}$ critically affects both the convergence behavior and the quality of the obtained solution. Although adaptive schemes such as line search or backtracking [38] can optimize the step size, they introduce substantial per-iteration computational overhead. Moreover, exhaustive or manual tuning is impractical for large-scale hybrid RIS systems, where each iteration involves high-complexity gradient computations in (28). To overcome these challenges, we employ a model-driven strategy that learns the step-size parameters via data training, referred to as the deep unfolded PGD model.

In the deep unfolding method, an iterative solver such as PGD is implemented as a layer-wise neural network, where each layer performs the mapping in (27), corresponding to one iteration of conventional PGD [16], [39]. This transformation converts a conventional fixed-step iterative solver into a trainable architecture that can be interpreted as a specialized DNN. To preserve the interpretability of the original algorithm while introducing flexibility, the unfolded model retains the same update structure but treats the step sizes as learnable parameters.

To enable gradient-based training, the hard projection steps used in PGD are replaced by differentiable approximations. In particular, to handle the binary phase constraint, we propose the following differentiable relaxation

for each intermediate phase $\tilde{\theta}_n$ obtained from the gradient update in (27)

$$\tilde{\theta}_n \leftarrow -\frac{\pi}{2} \tanh(\beta \cos(\tilde{\theta}_n)) + \frac{\pi}{2}, \quad n \in \mathcal{N}, \quad (29)$$

where $\beta > 0$ controls the sharpness of the relaxation. This mapping serves as a smooth surrogate for the hard binary phase projection and becomes sharper as β increases.

For active-set selection, the N_a RIS elements with the largest amplitudes are selected using a Top- N_a operation [40]. Since this hard selection is non-differentiable, we adopt a differentiable approximation during training based on a straight-through estimator (STE) [41], [42]. Specifically, a smooth sigmoid-based variable is used for gradient propagation during training, while at inference, a hard binary variable $g_n \in \{0, 1\}$ is used, where $g_n = 1$ indicates that the n th RIS element is selected as active and $g_n = 0$ otherwise. The amplitudes of all RIS elements are then written as

$$\tilde{\alpha}_n \leftarrow 1 + g_n(\tilde{\alpha}_n - 1), \quad n \in \mathcal{N}, \quad (30)$$

so that the selected active elements retain their amplitudes, whereas the remaining elements are assigned unit amplitude and operate as passive RIS elements.

To handle the RIS power-budget constraint in a gradient-compatible manner, we replace the hard scaling step in PGD with a ReLU-based normalization factor given by

$$s_{\text{RIS}} = 1 - \text{ReLU}\left(1 - \sqrt{\frac{P_r^{\max}}{P_r(\Phi)}}\right), \quad (31)$$

and update the active amplitudes as

$$\tilde{\alpha}_n \leftarrow s_{\text{RIS}} \tilde{\alpha}_n, \quad \forall n \in \mathcal{A}. \quad (32)$$

A similar normalization step is applied to enforce the BS transmit power constraint, yielding the scaling factor s_{BS} . These operations are applied sequentially after each gradient update.

With these differentiable approximations, the unfolded network can be trained end-to-end over J layers. The training loss function is defined as

$$\mathcal{L}(\eta_{\Phi}) = f(\Phi^{(J)}), \quad (33)$$

where $\Phi^{(J)}$ is the output of the final layer of the network, and $\eta_{\Phi} = \{\eta_{\Phi}^{(j)}\}_{j=0}^{J-1}$ denotes the trainable step sizes. Notice that the above loss $\mathcal{L}(\eta_{\Phi})$ depends on all the step sizes, i.e., $\{\eta_{\Phi}^{(j)}\}_{j=0}^{J-1}$, through $\Phi^{(J)}$, which is recursively determined by the layer-wise updates. Therefore, the unfolded PGD model is trained to learn the best set of step sizes. The proposed deep unfolded PGD method is summarized in Algorithm 2.

C. Overall Algorithm and Complexity Analysis

The overall procedure of the proposed method is summarized in Algorithm 3 and illustrated in Fig. 2. Starting from an initial feasible solution, the algorithm alternately updates the power allocation and the RIS coefficients until

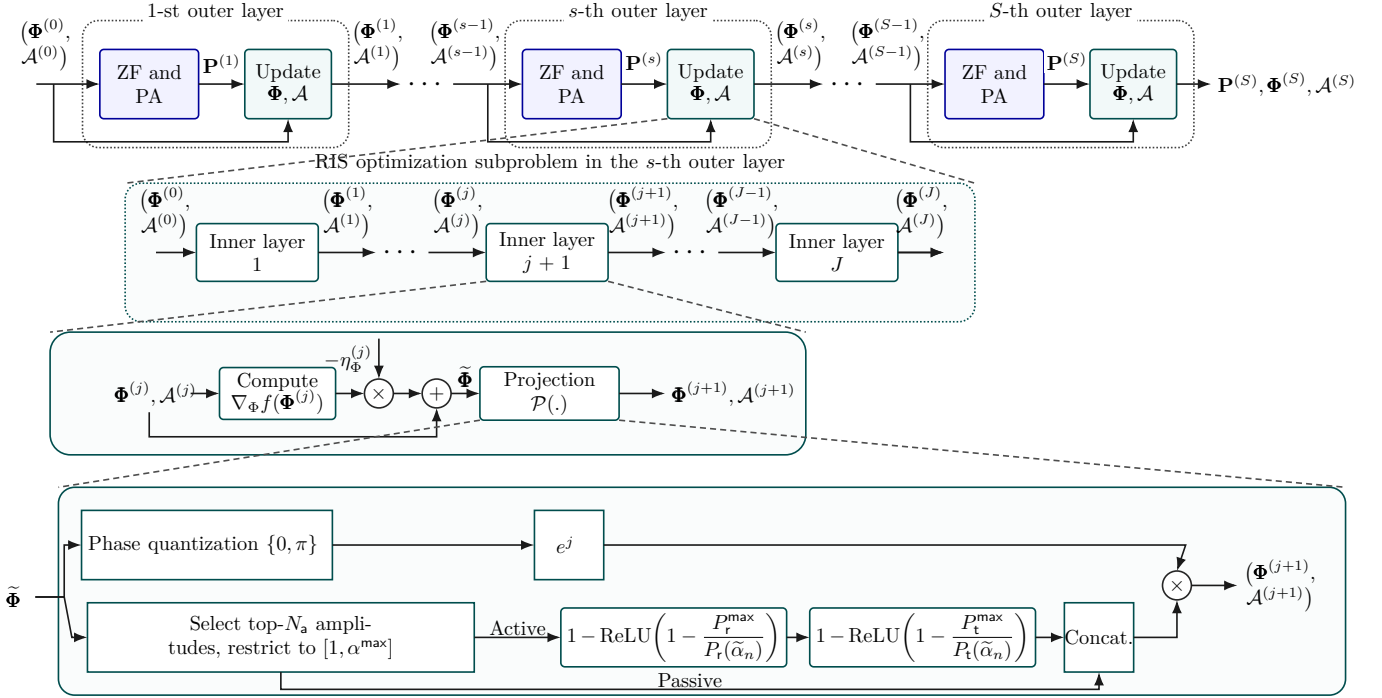


Fig. 2. Overall structure of the proposed algorithm.

Algorithm 2 Proposed Deep Unfolded PGD for hybrid RIS Optimization Subproblem (26)

Require: $\mathbf{H}_t, \mathbf{H}_r, \mathbf{P}$, trained step sizes $\{\eta_{\Phi}^{(j)}\}_{j=0}^{J-1}$

- 1: for $j = 0, \dots, J-1$ do
- 2: Compute gradient step: $\tilde{\Phi} \leftarrow \Phi^{(j)} - \eta_{\Phi}^{(j)} \nabla_{\Phi} f(\Phi^{(j)})$
- 3: Extract phases $\{\tilde{\theta}_n\}$ and amplitudes $\{\tilde{\alpha}_n\}$ from $\tilde{\Phi}$
- 4: Update each phase $\tilde{\theta}_n$ according to (29), $\forall n \in \mathcal{N}$
- 5: Select the set $\mathcal{A}^{(j+1)}$ via the top- N_a for $\tilde{\alpha}_n, \forall n \in \mathcal{N}$
- 6: Set $g_n = 1$ for $n \in \mathcal{A}^{(j+1)}$ and $g_n = 0$ for $n \in \mathcal{N} \setminus \mathcal{A}^{(j+1)}$
- 7: Update amplitudes based on (30)
- 8: Project $\tilde{\alpha}_n$ onto $[1, \alpha^{\max}]$, $\forall n \in \mathcal{A}^{(j+1)}$, (11e)
- 9: Scale $\tilde{\alpha}_n, \forall n \in \mathcal{A}^{(j+1)}$, through (31) and (32)
- 10: Repeat the above step with respect to the BS power
- 11: Update $\Phi^{(j+1)}$ using the updated $\{\tilde{\theta}_n\}$ and $\{\tilde{\alpha}_n\}$
- 12: end for
- 13: return $\Phi^* = \Phi^{(J)}$, and $\mathcal{A}^* = \mathcal{A}^{(J)}$

convergence based on Algorithms 1 and 2, respectively. Specifically, for fixed RIS coefficients, the power allocation matrix is first optimized. Then, for the resulting power allocation, the RIS coefficients and the active set are updated.

For the RIS updates, the dominant cost in each deep unfolded layer arises from the gradient computation in (28) and the subsequent projection operations. The gradient computation has complexity $\mathcal{O}(KN^2 + KNM + MK^2 + K^3 + NK^2)$. Since N is typically much larger than both K and M , the dominant term is $\mathcal{O}(KN^2)$. The projection steps, including phase projection, Top- N_a selection, amplitude clipping, and power normalization, require at most $\mathcal{O}(N \log N)$ operations, which is negligible compared with $\mathcal{O}(KN^2)$ for large N . Hence, the complexity of Al-

Algorithm 3 Deep Unfolded AO Framework for (18)

Require: $\mathbf{H}_t, \mathbf{H}_r$

- 1: Initialize $\mathbf{P}^{(0)}, \Phi^{(0)}, \mathcal{A}^{(0)}$, $s = 0$
- 2: for $s = 1, \dots, S$ do
- 3: Apply Algorithm 1 to obtain $\mathbf{P}^{(s)}$
- 4: Apply Algorithm 2 to obtain $\Phi^{(s)}, \mathcal{A}^{(s)}$
- 5: end for
- 6: return $\mathbf{P}^* = \mathbf{P}^{(S)}$, $\Phi^* = \Phi^{(S)}$, and $\mathcal{A}^* = \mathcal{A}^{(S)}$

gorithm 2 is approximated as $\mathcal{O}(JKN^2)$, where J denotes the number of unfolded layers. Since the power allocation step has lower complexity in the considered large N , the overall complexity of Algorithm 3 is dominated by the RIS updates and can be approximated as $\mathcal{O}(SJKN^2)$, where S denotes the number of outer AO iterations.

V. Conventional PGA Method

In the previous section, we proposed a deep unfolded AO-based solution to the main problem (11). To establish a rigorous benchmark, this section presents a baseline approach based on PGA, where the beamforming and RIS coefficient matrices are updated directly based on PGA to solve the original problem (11). Unlike the AO framework, PGA updates all variables simultaneously and therefore requires the constraints to be handled either through explicit projection operators. Since constraint (11d) cannot be directly enforced through projection, we incorporate it into the objective function using a penalty formulation [33]. Accordingly, problem (11) is reformulated as

$$\underset{\mathbf{F}, \Phi, \mathcal{A}}{\text{maximize}} \quad \text{EE} + \sum_{k=1}^K \omega_k \ln(\text{SE}_k - \text{SE}_k^{\min}) \quad (34a)$$

$$\text{subject to} \quad (11b) - (11c), (11e) - (11g), \quad (34b)$$

where $\omega_k > 0, \forall k$ are the weights of penalty terms. To apply the PGA method, we first derive the gradients of the objective function in (34) with respect to \mathbf{F} and Φ , whose closed-form expressions are provided in Lemma 1. Since the binary phase-shift constraint prevents the direct computation of the gradient with respect to Φ , we adopt the continuous relaxation described in Section IV-B2.

Lemma 1: The gradients of EE with respect to \mathbf{F} and Φ are given in (35) and (36), respectively. Similarly, the gradients of SE_k with respect to \mathbf{F} and Φ are provided in (37) and (38), respectively.

$$\begin{aligned} \nabla_{\mathbf{F}} \text{SE}_k &= \frac{2}{\ln 2} \left(\frac{\bar{\mathbf{H}}_k \mathbf{F}}{\text{tr}(\mathbf{F} \mathbf{F}^H \bar{\mathbf{H}}_k) + \hat{\sigma}_k^2} - \frac{\bar{\mathbf{H}}_k \mathbf{F}_{\bar{k}}}{\text{tr}(\mathbf{F}_{\bar{k}} \mathbf{F}_{\bar{k}}^H \bar{\mathbf{H}}_k) + \hat{\sigma}_k^2} \right), \quad (37) \\ \nabla_{\Phi} \text{SE}_k &= \frac{2}{\ln 2} \left(\frac{\mathbf{T}_k \Phi \mathbf{G}}{\text{tr}(\Phi^H \mathbf{T}_k \Phi \mathbf{G}) + \sigma_k^2} - \frac{\mathbf{T}_k \Phi \mathbf{G}_k}{\text{tr}(\Phi^H \mathbf{T}_k \Phi \mathbf{G}_k) + \sigma_k^2} \right) \circ \mathbf{I}_N. \quad (38) \end{aligned}$$

where

$$\bar{\mathbf{H}}_k \triangleq \mathbf{H}_t^H \Phi^H \mathbf{h}_{r,k} \mathbf{h}_{r,k}^H \Phi \mathbf{H}_t, \quad \mathbf{T}_k \triangleq \mathbf{h}_{r,k} \mathbf{h}_{r,k}^H \quad (39)$$

$$\bar{\mathbf{H}} \triangleq \mathbf{H}_t \mathbf{F} \mathbf{F}^H \mathbf{H}_t^H, \quad \bar{\mathbf{H}}_k \triangleq \mathbf{H}_t \mathbf{F}_{\bar{k}} \mathbf{F}_{\bar{k}}^H \mathbf{H}_t^H \quad (40)$$

$$\mathbf{G} \triangleq \tilde{\mathbf{H}} + \sigma_R^2 \mathbf{I}, \quad \mathbf{G}_k \triangleq \tilde{\mathbf{H}}_k + \sigma_R^2 \mathbf{I} \quad (41)$$

$$\hat{\sigma}_k^2 \triangleq \sigma_k^2 + \sigma_R^2 \|\mathbf{h}_{r,k}^H \Phi\|^2 = \sigma_k^2 + \sigma_R^2 \text{tr}(\Phi^H \mathbf{h}_{r,k} \mathbf{h}_{r,k}^H \Phi) \quad (42)$$

with $\mathbf{F}_{\bar{k}}$ obtained by replacing the k -th column of \mathbf{F} with all zeros. See Appendix A.

Using the above gradients, the corresponding PGA updates are given by

$$\hat{\Phi}^{(t+1)} = \Phi^{(t)} + \nu_{\Phi}^{(t)} \left(\nabla_{\Phi} \text{EE} + \sum_{k=1}^K \frac{\omega_k \cdot \nabla_{\Phi} \text{SE}_k}{\text{SE}_k - \text{SE}_k^{\min}} \right) \Big|_{\Phi=\Phi^{(t)}}, \quad (43)$$

$$\Phi^{(t+1)} = \Pi_{\Phi}(\hat{\Phi}^{(t+1)}), \quad (44)$$

$$\hat{\mathbf{F}}^{(t+1)} = \mathbf{F}^{(t)} + \nu_{\mathbf{F}}^{(t)} \left(\nabla_{\mathbf{F}} \text{EE} + \sum_{k=1}^K \frac{\omega_k \cdot \nabla_{\mathbf{F}} \text{SE}_k}{\text{SE}_k - \text{SE}_k^{\min}} \right) \Big|_{\mathbf{F}=\mathbf{F}^{(t)}}, \quad (45)$$

$$\mathbf{F}^{(t+1)} = \Pi_{\mathbf{F}}(\hat{\mathbf{F}}^{(t+1)}), \quad (46)$$

where Π_{Φ} and $\Pi_{\mathbf{F}}$ denote projection operators that enforce the constraints of problem (34). The projection Π_{Φ} follows

the same hard-projection procedure described in Section IV-B2. The projection $\Pi_{\mathbf{F}}$ enforces the BS transmit-power constraint in (11b) and the dynamic amplifier-power constraint in (11c).

VI. Simulation Results

In this section, we provide simulation results to demonstrate the proposed method. We consider a scenario where the BS and RIS are located at (0, 0, 10) m and (5, 45, 10) m, respectively. The $K = 4$ users are distributed within a circular region of radius 10 m centered at (0, 50, 0) m. This geometry represents a typical coverage-enhancement scenario in which the RIS assists users located in a clustered area with limited direct connectivity to the BS. The BS is equipped with a uniform linear array (ULA) of $M = 8$ antennas arranged along the x -axis with half-wavelength spacing. The RIS employs a uniform planar array (UPA) with $N = N_y N_z = 10 \times 10$ elements arranged in the y - z plane, also with half-wavelength spacing.

The carrier frequency is set to $f_c = 3.5$ GHz. The noise power spectral density is $N_0 = -174$ dBm/Hz, and the system bandwidth is 20 MHz, which results in a noise power of $\sigma_k^2 = \sigma_R^2 = -101$ dBm. The BS circuit power is fixed to $P_{c,BS} = 36.0$ dBm, and the power amplifier efficiency coefficients are set to $\xi = \zeta = 0.9$ [35]. Each RIS phase-shift controller consumes $P_{ps} = -5.0$ dBm, while each active element requires an additional bias power of $P_{dc} = -5.0$ dBm. The maximum amplitude coefficient of each active RIS element is set to $\alpha^{\max} = 100$. The minimum SE requirement for each user is set to $\text{SE}_k^{\min} = 0.1$ bits/s/Hz. Unless otherwise stated, we set the number of RIS elements to $N = 100$, with $N_a = 60$ active elements, and the BS and RIS transmit power budget to $P_t^{\max} = 30$ dBm and $P_r^{\max} = -10$ dBm, respectively. The BS-RIS and RIS-user channels are modeled as quasi-static Rician fading channels [8] with Rician factors of 4 and path-loss exponents 2. We assume that CSI is available for the channels under consideration, although CSI acquisition in practical RIS-assisted systems remains challenging. The deep unfolded PGD module is trained using Adam with a learning rate of 0.01, a batch size of 100, $J = 5$ unfolded layers, 400 training channels, and 100 epochs. Testing is performed over 100 channels. The initial step size is set to $\eta_{\Phi} = 0.5$.

$$\nabla_{\mathbf{F}} \text{EE} = 2 \frac{\left(\sum_{k=1}^K \frac{\bar{\mathbf{H}}_k \mathbf{F}}{\ln 2 \cdot (\text{tr}(\mathbf{F} \mathbf{F}^H \bar{\mathbf{H}}_k) + \hat{\sigma}_k^2)} - \sum_{k=1}^K \frac{\bar{\mathbf{H}}_k \mathbf{F}_{\bar{k}}}{\ln 2 \cdot (\text{tr}(\mathbf{F}_{\bar{k}} \mathbf{F}_{\bar{k}}^H \bar{\mathbf{H}}_k) + \hat{\sigma}_k^2)} \right) \cdot P_{\text{tot}} - \text{SE} \cdot \left(\frac{1}{\xi} \mathbf{F} + \frac{1}{\zeta} \mathbf{H}_t^H \Phi^H \Phi \mathbf{H}_t \mathbf{F} \right)}{(P_{\text{tot}})^2} \quad (35)$$

$$\nabla_{\Phi} \text{EE} = 2 \frac{\left(\sum_{k=1}^K \frac{\mathbf{T}_k \Phi \mathbf{G}}{\ln 2 \cdot (\text{tr}(\Phi^H \mathbf{T}_k \Phi \mathbf{G}) + \sigma_k^2)} - \sum_{k=1}^K \frac{\mathbf{T}_k \Phi \mathbf{G}_k}{\ln 2 \cdot (\text{tr}(\Phi^H \mathbf{T}_k \Phi \mathbf{G}_k) + \sigma_k^2)} \right) \cdot P_{\text{tot}} - \text{SE} \cdot \left(\frac{1}{\zeta} \Phi \mathbf{G} \right)}{(P_{\text{tot}})^2} \circ \mathbf{I}_N \quad (36)$$

To assess the effectiveness of the proposed deep unfolding-based AO (AO-DU) method presented in Algorithm 3, we compare it with the following benchmark schemes

- AO-PGD: Employs the same AO framework as the proposed method, but replaces the deep unfolding module with a conventional PGD algorithm to optimize the RIS coefficients.
- PGA: Directly solves problem (11) using the PGA method described in Section V.
- Fixed: Fixes the active element set \mathcal{A} and optimizes the remaining variables using the proposed AO-DU scheme.
- Random: Randomly generates a feasible set of RIS variables once and keeps them fixed during the subsequent power allocation.
- Fully-active: Assumes that all RIS elements are active and applies the AO-DU algorithm to solve the resulting optimization problem.
- Fully-passive: Assumes that all RIS elements are passive and solves the problem using the AO-DU algorithm.

Fig. 3 shows the convergence behavior of the solution algorithms for problem (11). It is observed that the proposed AO-DU method converges faster and achieves higher EE than AO-PGD and PGA. In particular, it yields a sharp increase in EE during the initial iterations and reaches a higher convergence point within fewer iterations. In contrast, the PGA method shows the slowest convergence and attains the lowest EE. Its performance increases gradually in the early iterations and converges to a significantly lower EE compared with the AO-based schemes. Furthermore, the non-smooth behavior of the AO-DU and AO-PGD curves stems from the AO structure, where the RIS update and the power allocation update are performed alternately. In particular, re-solving the power allocation subproblem via the Dinkelbach algorithm at each AO iteration can change the objective value abruptly, leading to the observed saw-tooth convergence pattern. Fig. 4 compares the proposed approximation \tilde{EE} in (17) with the exact EE in (16) for different values of the maximum RIS amplification power budget P_r^{\max} . Here, the EE values are obtained based on the solution in Algorithm 3. It is seen that the approximate EE closely follows the exact EE over the whole considered range of P_r^{\max} , confirming the tightness of the approximation. To further examine this, we also consider a stronger RIS-user channel by reducing the RIS-user path loss by 10 dB. In this case, the gap becomes slightly larger, since the term $\sigma_R^2 \|\mathbf{h}_{r,k}^H \Phi_a\|^2$ increases. Nevertheless, the mismatch remains relatively small. It can also be seen that, as P_r^{\max} increases, the approximate EE decreases because the denominator of \tilde{EE} explicitly contains P_r^{\max} , whereas in the exact EE, the actual RIS dynamic power remains much smaller due to the amplitude constraint (11e). Overall, the results confirm that the proposed approximation is well justified for practical low-power RIS systems. Fig. 5 shows the EE

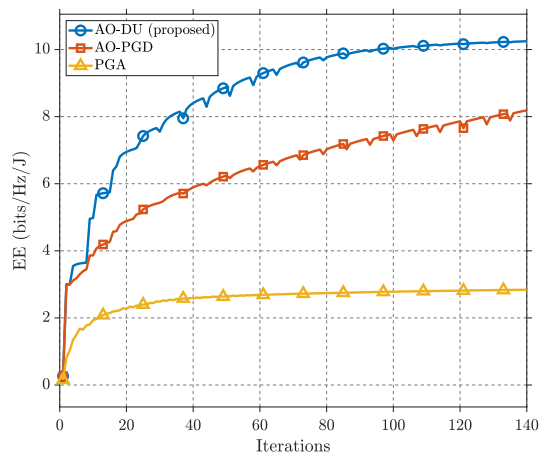


Fig. 3. Convergence of AO-DU and AO-PGD with $J = 5$, $I = 2$, and $N_a = 10$.

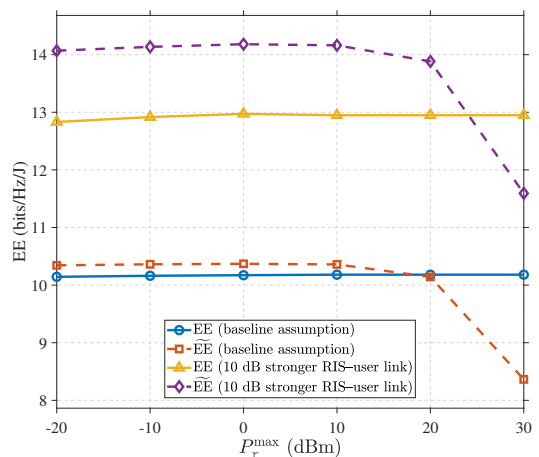


Fig. 4. Exact EE and approximate \tilde{EE} versus P_r^{\max} for the baseline and stronger RIS-user channel.

versus the number of active elements N_a for different RIS dynamic power budgets P_r^{\max} . Here, $N_a = 0$ corresponds to the fully passive RIS, while $N_a = 100$ corresponds to the fully active RIS. It is observed that for all considered power budgets, increasing N_a from zero improves the EE, since the active elements provide additional amplification gain and enhance the achievable rate. This improvement is already significant even with a small number of active elements. For example, at $N_a = 10$, the EE reaches nearly 80% of its maximum value. However, as N_a increases further, the EE gain gradually saturates and may even decrease for limited RIS power budgets. This is because the available RIS dynamic power must be shared among more active elements, which reduces the amplification gain of each active element. This effect can be clearly seen for $P_r^{\max} = -10$ and 0 dBm, while for $P_r^{\max} = 10$ dBm, the EE continues to increase over a wider range of N_a .

Fig. 6 illustrates the impact of the total dynamic power budget, defined as the sum of the BS transmit power budget and the RIS dynamic amplifier power budget, i.e.,

$$P_{\text{tot}}^{\text{dyn}} = P_{\text{t}}^{\max} + P_r^{\max}. \quad (47)$$

This quantity represents the total available dynamic power that can be distributed between the BS and the RIS.

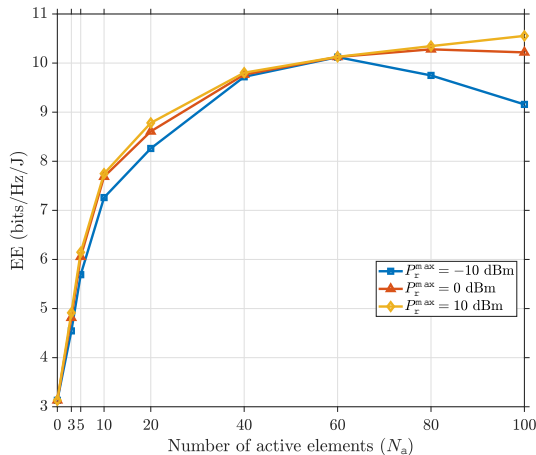


Fig. 5. EE versus N_a for $N = 100$ under different RIS dynamic power budgets P_r^{\max} .

To examine the power-sharing effect, we proportionally allocate the total dynamic power between the BS and the RIS using a power-sharing coefficient τ , such that

$$P_r^{\max} = \tau P_{\text{tot}}^{\text{dyn}}, \quad P_t^{\max} = (1-\tau)P_{\text{tot}}^{\text{dyn}}, \quad 0 \leq \tau \leq 1, \quad (48)$$

where τ denotes the fraction of dynamic power allocated to the RIS. We evaluate $\tau \in [0, 0.99]$ for a fixed total dynamic power budget $P_{\text{tot}}^{\text{dyn}} = 30$ dBm under three configurations: fully active RIS, fully passive RIS, and hybrid RIS.

It is observed from Fig. 6 that the EE of the fully passive RIS remains constant over the whole range of τ , since the passive RIS does not use dynamic amplification. For the hybrid and fully active RIS architectures, increasing τ initially improves the EE. However, with only a small portion of the total dynamic power, the hybrid RIS can already approach its maximum EE, since its limited number of active elements can effectively exploit the available amplification gain. In contrast, fully active RIS achieves lower EE at small values of τ , but can benefit more from increasing τ because the additional RIS power is distributed among a larger number of active elements. As τ increases further, the EE gain becomes limited and may even decrease due to the power-sharing trade-off between the BS and the RIS. In this regime, less power remains available at the BS, while the RIS cannot fully exploit the additional power because of the active-element amplification-gain constraint. Overall, the results show that allocating only a small fraction of the total dynamic power to the RIS is more energy-efficient.

Figs. 7a and 7b show the EE and SE versus the BS transmit power budget, respectively. It is observed that both EE and SE increase with P_t^{\max} at first and then become nearly flat when P_t^{\max} is sufficiently large. This is because, under EE maximization, the BS does not necessarily use all the available transmit power. Instead, the transmit power is chosen to balance the achieved rate and the total power consumption. Therefore, when P_t^{\max} becomes sufficiently large, further increasing the transmit power budget provides only marginal improvement. It is also observed that the proposed AO-DU

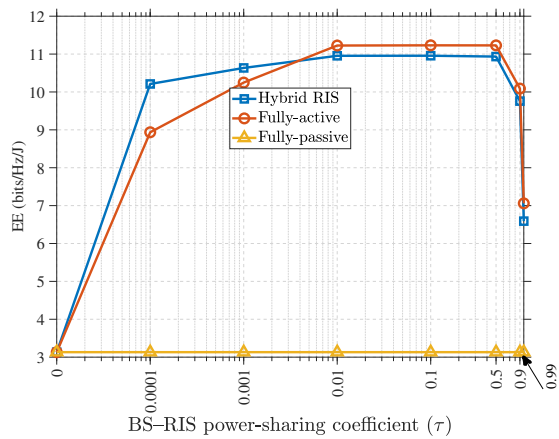


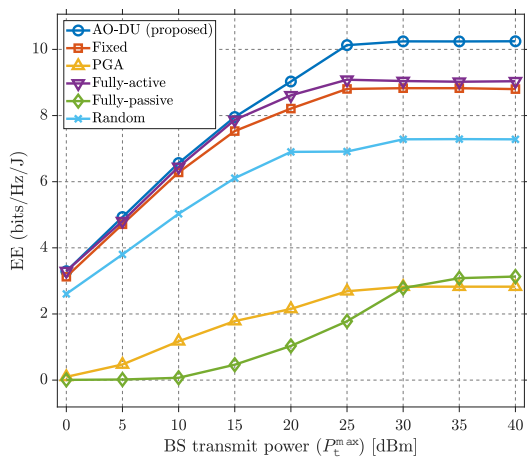
Fig. 6. EE versus the power-sharing coefficient τ under a fixed total dynamic power budget (BS and RIS combined).

scheme achieves the best performance in both figures over the whole considered transmit power range. The Fixed scheme performs worse, which highlights the importance of optimizing the active-element positions. The Fully-Active scheme is also inferior to the proposed AO-DU design, although it performs better than the Fixed scheme. The Random scheme performs worse than these optimized schemes, while the Fully-Passive scheme has much lower performance, around three times lower than the proposed hybrid RIS in the high-power regime in terms of EE. The PGA benchmark performs poorly and becomes even worse than the Fully-Passive scheme when P_t^{\max} is large.

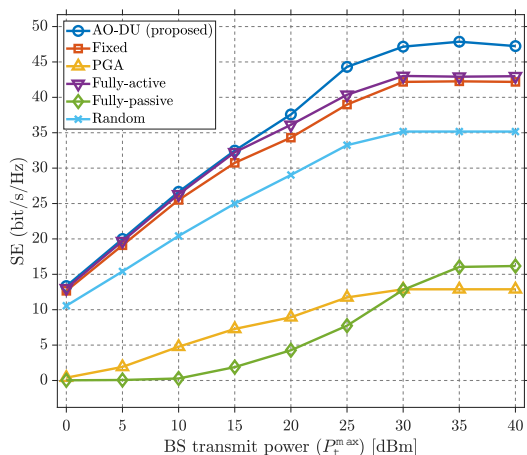
VII. Conclusion

We addressed an EE maximization problem in a hybrid RIS-assisted MU-MISO downlink system under practical hardware constraints, including BS and RIS power budgets, active-element amplifier gain limits, amplification noise, and binary phase-shift control. The problem jointly optimizes the BS transmit beamforming, the active/passive mode selection, their amplification gains, and the RIS phase shifts. To solve this problem, we developed a deep unfolded AO-based framework in which the BS beamforming subproblem is handled via ZF with closed-form power allocation, while the RIS subproblem is addressed using a model-driven deep unfolding approach.

The numerical results showed that the proposed method achieves higher EE and faster convergence than the considered benchmark schemes. The results also confirmed that the hybrid RIS architecture achieves a more favorable rate-energy trade-off than the fully passive and fully active configurations and that only a limited number of active elements and a small portion of the dynamic power budget need to be assigned to the RIS to approach the best performance. These observations highlight the effectiveness of combining hybrid RIS design with deep unfolding for practical EE optimization. Future work may consider more general network settings, including multiple hybrid RIS, and joint power sharing among the BS and multiple RISs.



(a) EE versus BS transmit power budget.



(b) SE versus BS transmit power budget.

Fig. 7. EE and SE versus the BS transmit power budget for different RIS configurations with $N = 100$ elements.

Appendix A Proof of Lemma 1

We first compute the gradient of EE by applying the chain rule, which gives

$$\nabla_{\mathbf{F}} \text{EE} = \frac{\nabla_{\mathbf{F}} \text{SE} \cdot P_{\text{tot}} - \text{SE} \cdot \nabla_{\mathbf{F}} P_{\text{tot}}}{(P_{\text{tot}})^2} \quad (49)$$

$$\nabla_{\Phi} \text{EE} = \frac{\nabla_{\Phi} \text{SE} \cdot P_{\text{tot}} - \text{SE} \cdot \nabla_{\Phi} P_{\text{tot}}}{(P_{\text{tot}})^2} \quad (50)$$

To derive the gradient of SE, we first obtain the gradient of SE_k and then sum the resulting per-user gradients over all users. Based on (6), SE_k can be reformulated as

$$\begin{aligned} \text{SE}_k &= \log_2(1 + \gamma_k) \\ &= \log_2 \left(\frac{\sum_{i=1}^K \left| \mathbf{h}_{r,k}^H \Phi \mathbf{H}_t \mathbf{f}_i \right|^2 + \hat{\sigma}_k^2}{\sum_{i \neq k}^K \left| \mathbf{h}_{r,k}^H \Phi \mathbf{H}_t \mathbf{f}_i \right|^2 + \hat{\sigma}_k^2} \right) \\ &= \log_2 \left(\frac{\text{tr} \left(\mathbf{F} \mathbf{F}^H \mathbf{H}_t^H \Phi^H \mathbf{h}_{r,k} \mathbf{h}_{r,k}^H \Phi \mathbf{H}_t \right) + \hat{\sigma}_k^2}{\text{tr} \left(\mathbf{F}_k \mathbf{F}_k^H \mathbf{H}_t^H \Phi^H \mathbf{h}_{r,k} \mathbf{h}_{r,k}^H \Phi \mathbf{H}_t \right) + \hat{\sigma}_k^2} \right) \\ &= \log_2 \left(\frac{\text{tr} \left(\mathbf{F} \mathbf{F}^H \bar{\mathbf{H}}_k \right) + \hat{\sigma}_k^2}{\text{tr} \left(\mathbf{F}_k \mathbf{F}_k^H \bar{\mathbf{H}}_k \right) + \hat{\sigma}_k^2} \right) \end{aligned} \quad (51)$$

$$\begin{aligned} &= \log_2 \left(\frac{\text{tr} \left(\Phi^H \mathbf{h}_{r,k} \mathbf{h}_{r,k}^H \Phi \mathbf{H}_t \mathbf{F} \mathbf{F}^H \mathbf{H}_t^H \right) + \hat{\sigma}_k^2}{\text{tr} \left(\Phi^H \mathbf{h}_{r,k} \mathbf{h}_{r,k}^H \Phi \mathbf{H}_t \mathbf{F}_k \mathbf{F}_k^H \mathbf{H}_t^H \right) + \hat{\sigma}_k^2} \right) \\ &= \log_2 \left(\frac{\text{tr} \left(\Phi^H \mathbf{T}_k \Phi \tilde{\mathbf{H}} \right) + \sigma_k^2 + \sigma_{\text{R}}^2 \text{tr} \left(\Phi^H \mathbf{T}_k \Phi \right)}{\text{tr} \left(\Phi^H \mathbf{T}_k \Phi \tilde{\mathbf{H}}_k \right) + \sigma_k^2 + \sigma_{\text{R}}^2 \text{tr} \left(\Phi^H \mathbf{T}_k \Phi \right)} \right) \\ &= \log_2 \left(\frac{\text{tr} \left(\Phi^H \mathbf{T}_k \Phi \left(\tilde{\mathbf{H}} + \sigma_{\text{R}}^2 \mathbf{I} \right) \right) + \sigma_k^2}{\text{tr} \left(\Phi^H \mathbf{T}_k \Phi \left(\tilde{\mathbf{H}}_k + \sigma_{\text{R}}^2 \mathbf{I} \right) \right) + \sigma_k^2} \right) \\ &= \log_2 \left(\frac{\text{tr} \left(\Phi^H \mathbf{T}_k \Phi \mathbf{G} \right) + \sigma_k^2}{\text{tr} \left(\Phi^H \mathbf{T}_k \Phi \mathbf{G}_k \right) + \sigma_k^2} \right), \end{aligned} \quad (52)$$

where $\bar{\mathbf{H}}_k$, $\tilde{\mathbf{H}}$, and $\tilde{\mathbf{H}}_k$ are defined in Lemma 1.

Using (51), the gradient of SE_k with respect to \mathbf{F} is obtained as [43]

$$\begin{aligned} \nabla_{\mathbf{F}} \text{SE}_k &= \frac{\partial}{\partial \mathbf{F}^*} \log_2 \left(\text{tr} \left(\mathbf{F} \mathbf{F}^H \bar{\mathbf{H}}_k \right) + \hat{\sigma}_k^2 \right) \\ &\quad - \frac{\partial}{\partial \mathbf{F}^*} \log_2 \left(\text{tr} \left(\mathbf{F}_k \mathbf{F}_k^H \bar{\mathbf{H}}_k \right) + \hat{\sigma}_k^2 \right) \\ &= 2 \frac{\bar{\mathbf{H}}_k \mathbf{F}}{\ln 2 \left(\text{tr} \left(\mathbf{F} \mathbf{F}^H \bar{\mathbf{H}}_k \right) + \hat{\sigma}_k^2 \right)} \\ &\quad - 2 \frac{\bar{\mathbf{H}}_k \mathbf{F}_k}{\ln 2 \left(\text{tr} \left(\mathbf{F}_k \mathbf{F}_k^H \bar{\mathbf{H}}_k \right) + \hat{\sigma}_k^2 \right)}. \end{aligned} \quad (53)$$

Similarly, using (52), the gradient of SE_k with respect to Φ is given by

$$\begin{aligned} \nabla_{\Phi} \text{SE}_k &= \frac{\partial}{\partial \Phi^*} \log_2 \left(\text{tr} \left(\Phi^H \mathbf{T}_k \Phi \mathbf{G} \right) + \sigma_k^2 \right) \\ &\quad - \frac{\partial}{\partial \Phi^*} \log_2 \left(\text{tr} \left(\Phi^H \mathbf{T}_k \Phi \mathbf{G}_k \right) + \sigma_k^2 \right) \\ &= 2 \frac{\mathbf{T}_k \Phi \mathbf{G}}{\ln 2 \left(\text{tr} \left(\Phi^H \mathbf{T}_k \Phi \mathbf{G} \right) + \sigma_k^2 \right)} \circ \mathbf{I}_N \\ &\quad - 2 \frac{\mathbf{T}_k \Phi \mathbf{G}_k}{\ln 2 \left(\text{tr} \left(\Phi^H \mathbf{T}_k \Phi \mathbf{G}_k \right) + \sigma_k^2 \right)} \circ \mathbf{I}_N. \end{aligned} \quad (54)$$

Consequently, the gradients of SE with respect to \mathbf{F} and Φ are given, respectively, by

$$\nabla_{\mathbf{F}} \text{SE} = \sum_{k=1}^K \nabla_{\mathbf{F}} \text{SE}_k, \quad (55)$$

$$\nabla_{\Phi} \text{SE} = \sum_{k=1}^K \nabla_{\Phi} \text{SE}_k. \quad (56)$$

The gradient of P_{tot} , based on (10), is given by

$$\nabla_{\mathbf{F}} P_{\text{tot}} = \frac{1}{\xi} \mathbf{F} + \frac{1}{\zeta} \mathbf{H}_t^H \Phi^H \Phi \mathbf{H}_t \mathbf{F}, \quad (57)$$

$$\nabla_{\Phi} P_{\text{tot}} = \frac{1}{\zeta} \left(\Phi \left(\tilde{\mathbf{H}} + \sigma_{\text{R}}^2 \mathbf{I} \right) \right) \circ \mathbf{I}_N = \frac{1}{\zeta} \Phi \mathbf{G} \circ \mathbf{I}_N. \quad (58)$$

Finally, substituting (55) and (57) into (49) yields (35). Similarly, substituting (56) and (58) into (50) gives (36), which completes the proof of Lemma 1.

References

- [1] P. Mobaraki, N. T. Nguyen, and M. Juntti, "Deep unfolding-empowered energy efficiency optimization in RIS-assisted wireless communications," ser. *IoT '24*, Oulu, Finland, 2025, p. 238–243. [Online]. Available: <https://doi.org/10.1145/3703790.3703830>
- [2] H. Wymeersch, J. He, B. Denis, A. Clemente, and M. Juntti, "Radio localization and mapping with reconfigurable intelligent surfaces: Challenges, opportunities, and research directions," *IEEE Veh. Technol. Mag.*, vol. 15, no. 4, pp. 52–61, Dec. 2020.
- [3] A. Umer, I. Mürsepp, M. M. Alam, and H. Wymeersch, "Reconfigurable intelligent surfaces in 6G radio localization: A survey of recent developments, opportunities, and challenges," *IEEE Commun. Surveys Tuts.*, vol. 27, no. 6, pp. 3526–3560, Dec. 2025.
- [4] M. Di Renzo, A. Zappone, M. Debbah, M.-S. Alouini, C. Yuen, J. de Rosny, and S. Tretyakov, "Smart radio environments empowered by reconfigurable intelligent surfaces: How it works, state of research, and the road ahead," *IEEE J. Sel. Areas Commun.*, vol. 38, no. 11, pp. 2450–2525, Nov. 2020.
- [5] C. Huang, A. Zappone, G. C. Alexandropoulos, M. Debbah, and C. Yuen, "Reconfigurable intelligent surfaces for energy efficiency in wireless communication," *IEEE Trans. Wireless Commun.*, vol. 18, no. 8, pp. 4157–4170, Aug. 2019.
- [6] Z. Zhang, L. Dai, X. Chen, C. Liu, F. Yang, R. Schober, and H. V. Poor, "Active RIS vs. passive RIS: Which will prevail in 6G?" *IEEE Trans. Commun.*, vol. 71, no. 3, pp. 1707–1725, Mar. 2023.
- [7] K. Liu, Z. Zhang, L. Dai, S. Xu, and F. Yang, "Active reconfigurable intelligent surface: Fully-connected or sub-connected?" *IEEE Commun. Lett.*, vol. 26, no. 1, pp. 167–171, Jan. 2022.
- [8] N. T. Nguyen, Q.-D. Vu, K. Lee, and M. Juntti, "Hybrid relay-reflecting intelligent surface-assisted wireless communications," *IEEE Trans. Veh. Technol.*, vol. 71, no. 6, pp. 6228–6244, Jun. 2022.
- [9] D. V. Q. Rodrigues and T. Singh, "Efficient power allocation strategies in hybrid active-passive reconfigurable intelligent surfaces," *IEEE Commun. Lett.*, vol. 28, no. 1, pp. 113–117, Jan. 2024.
- [10] W. Lyu, Y. Xiu, S. Yang, C. Yuen, and Z. Zhang, "Energy-efficient cell-free network assisted by hybrid RISs," *IEEE Wireless Commun. Lett.*, vol. 12, no. 4, pp. 718–722, Apr. 2023.
- [11] D. Choudhury and A. K. Sah, "Energy-efficient beamforming optimization for hybrid-RIS-aided massive MIMO networks," *IEEE Trans. Veh. Technol.*, pp. 1–13, 2026.
- [12] A. Huang, X. Mu, L. Guo, and G. Zhu, "Hybrid active-passive RIS transmitter-enabled energy-efficient multi-user communications," *IEEE Trans. Wireless Commun.*, vol. 23, no. 9, pp. 10 653–10 666, Sep. 2024.
- [13] N. P. Le and M.-S. Alouini, "Distributed hybrid active-passive RIS-assisted THz wireless systems: Performance analysis and optimization," *IEEE Trans. Commun.*, vol. 73, no. 2, pp. 1399–1414, Feb. 2025.
- [14] S. Xie, S. Gong, H. Liu, T. Yu, N. Zhao, and C. Xing, "Energy efficiency optimization for hybrid active-passive RIS-aided communications: A novel dynamic subarray-based architecture," *IEEE Trans. Wireless Commun.*, vol. 25, pp. 8228–8245, 2025.
- [15] Q. Peng, Q. Wu, G. Chen, R. Liu, S. Ma, and W. Chen, "Hybrid active-passive IRS-assisted energy-efficient wireless communication," *IEEE Commun. Lett.*, vol. 27, no. 8, pp. 2202–2206, Aug. 2023.
- [16] J. R. Hershey, J. Le Roux, and F. Wenzler, "Deep unfolding: Model-based inspiration of novel deep architectures," *arXiv preprint arXiv:1409.2574*, Sep. 2014.
- [17] N. Shlezinger, S. Segarra, Y. Zhang, D. Avrahami, Z. Davidov, T. Routtenberg, and Y. C. Eldar, "Deep unfolding: Recent developments, theory, and design guidelines," *arXiv preprint arXiv:2512.03768*, Mar. 2025.
- [18] Y. Ju, S. Gong, H. Liu, C. Xing, J. An, and Y. Li, "Beamforming optimization for hybrid active-passive RIS-assisted wireless communications: A rate-maximization perspective," *IEEE Trans. Commun.*, vol. 72, no. 9, pp. 5428–5442, Sep. 2024.
- [19] Z. Kang, C. You, and R. Zhang, "Active-passive IRS-aided wireless communication: New hybrid architecture and elements allocation optimization," *IEEE Trans. Wireless Commun.*, vol. 23, no. 4, pp. 3450–3464, Apr. 2024.
- [20] N. T. Nguyen, V.-D. Nguyen, H. Van Nguyen, Q. Wu, A. Tölli, S. Chatzinotas, and M. Juntti, "Fairness enhancement of UAV systems with hybrid active-passive RIS," *IEEE Trans. Wireless Commun.*, vol. 23, no. 5, pp. 4379–4396, May 2024.
- [21] H. Xie, D. Li, and B. Gu, "Exploring hybrid active-passive RIS-aided MEC systems: From the mode-switching perspective," *IEEE Trans. Wireless Commun.*, vol. 23, no. 9, pp. 11 291–11 308, Sep. 2024.
- [22] N. T. Nguyen, V.-D. Nguyen, Q. Wu, A. Tölli, S. Chatzinotas, and M. Juntti, "Hybrid active-passive reconfigurable intelligent surface-assisted multi-user MISO systems," in *Proc. IEEE Works. on Sign. Proc. Adv. in Wirel. Comms.*, Oulu, Finland, Jul. 2022, pp. 1–5.
- [23] M. Soleymani, A. Zappone, E. Jorswieck, M. Di Renzo, and I. Santamaria, "Spectral-energy efficiency tradeoff of nearly-passive RIS in mimo urlc downlink: Diagonal versus beyond diagonal," *IEEE Wireless Commun. Lett.*, vol. 15, pp. 890–894, Dec. 2025.
- [24] R. K. Fotock, A. Zappone, and M. Di Renzo, "Energy efficiency optimization in RIS-aided wireless networks: Active versus nearly-passive RIS with global reflection constraints," *IEEE Trans. Commun.*, vol. 72, no. 1, pp. 257–272, Jan. 2024.
- [25] K. Stylianopoulos and G. C. Alexandropoulos, "Online RIS configuration learning for arbitrary large numbers of 1-bit phase resolution elements," in *Proc. IEEE Works. on Sign. Proc. Adv. in Wirel. Comms.*, Oulu, Finland, Jul. 2022, pp. 1–5.
- [26] J. Sang, J. Lan, M. Zhou, B. Gao, W. Tang, X. Li, X. Yi, and S. Jin, "Quantized phase alignment by discrete phase shifts for reconfigurable intelligent surface-assisted communication systems," *IEEE Trans. Veh. Technol.*, vol. 73, no. 4, pp. 5259–5275, Apr. 2024.
- [27] A. Zappone, M. Di Renzo, X. Xi, and M. Debbah, "On the optimal number of reflecting elements for reconfigurable intelligent surfaces," *IEEE Wireless Communications Letters*, vol. 10, no. 3, pp. 464–468, Mar. 2021.
- [28] S. Gong, Y. Ju, H. Liu, L. Liu, and C. Xing, "Hybrid active-passive RIS-empowered secure communications: Joint architecture design and beamforming optimization," *IEEE Trans. Commun.*, vol. 73, no. 7, pp. 5094–5110, Jul. 2025.
- [29] R. Zhong, Y. Liu, X. Mu, Y. Chen, and L. Song, "AI-empowered RIS-assisted NOMA networks: Deep learning or reinforcement learning?" *IEEE J. Sel. Areas Commun.*, vol. 40, no. 1, pp. 182–196, Jan. 2022.
- [30] M. Wu, Z. Gao, Y. Huang, Z. Xiao, D. W. K. Ng, and Z. Zhang, "Deep learning-based rate-splitting multiple access for reconfigurable intelligent surface-aided tera-hertz massive MIMO," *IEEE J. Sel. Areas Commun.*, vol. 41, no. 5, pp. 1431–1451, May 2023.
- [31] A. Balatsoukas-Stimming and C. Studer, "Deep unfolding for communications systems: A survey and some new directions," in *Proc. IEEE Workshop Signal Process. Syst. (SiPS)*, Nanjing, China, Oct. 2019, pp. 266–271.
- [32] J. Zhang, M. Liu, J. Tang, N. Zhao, D. Niyato, and X. Wang, "Joint design for RIS-aided ISAC via deep unfolding learning," *IEEE Trans. on Cogn. Commun. Netw.*, vol. 11, no. 1, pp. 349–361, Feb. 2025.
- [33] N. T. Nguyen, L. V. Nguyen, N. Shlezinger, Y. C. Eldar, A. L. Swindlehurst, and M. Juntti, "Joint communications and sensing hybrid beamforming design via deep unfolding," *IEEE J. Sel. Topics Signal Process.*, vol. 18, no. 5, pp. 901–916, Jul. 2024.
- [34] K. Zhi, C. Pan, H. Ren, K. K. Chai, and M. El-Kashlan, "Active RIS versus passive RIS: Which is superior with the same power budget?" *IEEE Commun. Lett.*, vol. 26, no. 5, pp. 1150–1154, May 2022.
- [35] K. Ntougias, S. Chatzinotas, and I. Krikidis, "Hybrid RIS with sub-connected active partitions: Performance analysis and transmission design," *IEEE Trans. Wireless Commun.*, vol. 24, no. 8, pp. 6705–6721, Aug. 2025.
- [36] W. Dinkelbach, "On nonlinear fractional programming," *Management Science*, vol. 13, no. 7, pp. 492–498, 1967.
- [37] K. B. Petersen, M. S. Pedersen et al., "The matrix cookbook," Technical University of Denmark, p. 510, 2008.
- [38] S. P. Boyd and L. Vandenberghe, *Convex optimization*. Cambridge University Press, 2004.
- [39] S. Deka, K. Deka, N. T. Nguyen, S. Sharma, V. Bhatia, and N. Rajatheva, "Comprehensive review of deep unfolding tech-

- niques for next-generation wireless communication systems,” arXiv preprint arXiv:2502.05952, Feb. 2025.
- [40] S. Shi, X. Chu, K. C. Cheung, and S. See, “Understanding top-k sparsification in distributed deep learning,” arXiv preprint arXiv:1911.08772, Nov. 2019.
- [41] Y. Bengio, N. Léonard, and A. Courville, “Estimating or propagating gradients through stochastic neurons for conditional computation,” arXiv preprint arXiv:1308.3432, Aug. 2013.
- [42] P. Yin, J. Lyu, S. Zhang, S. Osher, Y. Qi, and J. Xin, “Understanding straight-through estimator in training activation-quantized neural nets,” arXiv preprint arXiv:1903.05662, Mar. 2019.
- [43] A. Hjørungnes, *Complex-valued matrix derivatives: With applications in signal processing and communications*. Cambridge University Press, 2011.